applied optics

# Optimized actuators for ultrathin deformable primary mirrors

Marie Laslandes,[1] Keith Patterson,[2] and Sergio Pellegrino[1,*]

[1]California Institute of Technology, 1200 E. California Blvd, Pasadena, California 91125, USA
[2]Jet Propulsion Laboratory, California Institute of Technology, 4800 Oak Grove Drive, Pasadena, California 91109, USA
*Corresponding author: sergiop@caltech.edu

Received 7 January 2015; revised 10 April 2015; accepted 16 April 2015; posted 17 April 2015 (Doc. ID 231885); published 20 May 2015

**A novel design and selection scheme for surface-parallel actuators for ultrathin, lightweight mirrors is presented. The actuation system consists of electrodes printed on a continuous layer of piezoelectric material bonded to an optical-quality substrate. The electrodes provide almost full coverage of the piezoelectric layer, in order to maximize the amount of active material that is available for actuation, and their shape is optimized to maximize the correctability and stroke of the mirror for a chosen number of independent actuators and for a dominant imperfection mode. The starting point for the design of the electrodes is the observation that the correction of a figure error that has at least two planes of mirror symmetry is optimally done with twin actuators that have the same optimized shape but are rotated through a suitable angle. Additional sets of optimized twin actuators are defined by considering the intersection between the twin actuators, and hence an arbitrarily fine actuation pattern can be generated. It is shown that this approach leads to actuator systems with better performance than simple, geometrically based actuators. Several actuator patterns to correct third-order astigmatism aberrations are presented, and an experimental demonstration of a 41-actuator mirror is also presented.** 

***OCIS codes:*** (110.1080) Active or adaptive optics; (110.1220) Apertures; (110.6770) Telescopes.

http://dx.doi.org/10.1364/AO.54.004937

## 1. INTRODUCTION

Deformable mirrors are able to correct the wavefront shape in optical instruments for a variety of applications, including astronomy [1], high-energy lasers [2], microscopy [3], and ophthalmology [4]. Each application has different requirements, in terms of precision of correction and the amplitude, spatial frequency and temporal frequency of the wavefront error to be corrected [5].

There are three basic technologies for deformable mirrors [6]: surface-normal actuation, surface-parallel actuation, and boundary actuation. *Surface-normal* actuators apply forces perpendicular to the optical surface; an array of push/pull actuators produces local displacements and slopes [7] by reacting against a backing structure. It is an efficient solution to compensate for relatively high spatial frequencies and low amplitude errors. *Surface-parallel* actuated systems consist of an active material laminated to a mirror face-sheet; the in-plane stretching or contraction of the active material causes the mirror to bend [8–11]. This solution does not require any backing structure and hence is suited to lighter mirrors and to the correction of larger amplitude errors. Alternative implementations have adopted discrete actuators embedded in a lightweighted structure [12]. Systems with *boundary actuators* use forces and moments along the edge of the mirror to bend the optical surface [13]. This approach minimizes the actuator print-through and is ideal to compensate for low spatial frequency errors with a relatively small number of actuators.

Active primary mirrors in earth-based telescopes have already enabled the emergence of very large apertures [14] and the future development of larger space-based observatories will require novel active primary mirror technologies [15]. This paper presents the further development of a recently proposed concept for thin deformable mirrors that promises to drastically reduce the mass, density, and cost of future telescopes [10]. Mirrors based on this approach are lightweight, relatively inexpensive, and provide a sufficiently large shape correction capability to allow the use of nominally identical, spherical mirror segments in large segmented primary apertures. Earlier studies [9] have shown that 1 m diameter spherical segments forming a 10 m diameter segmented aperture with a focal length of 10 m would require a correction bandwidth of the order of 250 μm to achieve the required shape in all segments. Accurate shape control would also allow active compensation for thermal effects and long-term effects such as creep and aging of the mirror materials.

The basic concept, presented in Fig. 1, consists of a laminated mirror based on surface-parallel actuation. The mirror is composed of a thin and stiff optical-quality substrate with a continuous layer of piezoelectric material bonded to the back. This piezoelectric layer is covered by patterned electrodes on one face and by a continuous ground layer on the other face. As an alternative, several piezoelectric layers could be used, instead of a single one.

Recent studies have addressed the manufacturing process and have explored and optimized different material choices, leading to two different solutions. The first solution [11] uses microfabrication techniques: the substrate is a wafer of single-crystal silicon or glass and the active layer is formed from a piezopolymer, P(VDF-TrFE). A reflective metallic layer with thickness chosen such as to achieve thermal balancing of the laminate (i.e., to minimize thermally induced bending) is deposited on the substrate. This approach has been demonstrated to provide high optical quality mirrors with a dynamic range of tens of micrometers. The optical diameter accessible with such a technology is limited by the manufacturing capabilities of microfabrication, typically 100–200 mm. The second solution [16] uses a simpler manufacturing process based on carbon fiber reinforced plastic composite technology. The substrate is an ultrathin composite shell and the active layer is made of a piezoceramic, PZT. It is suitable for larger mirrors and is able to correct wavefront errors of the order of millimeters. Nevertheless, producing composite shells of optical quality is challenging due to fiber print-through and the residual stresses resulting from curing.

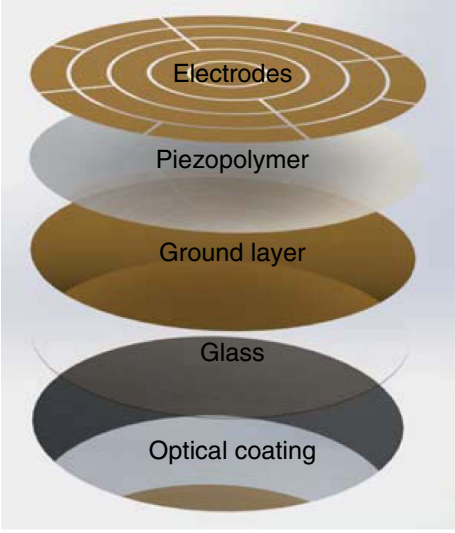


**Fig. 1.** Exploded view of the deformable mirror concept, showing separate layers (from [11]).

The active layer designs used in previous studies were mostly based on geometric intuition, with three main electrode patterns, Fig. 2. Unimorph and bimorph mirrors are classically designed with a keystone layout in which the actuators are arranged in rings and divided into angular domains [17]. Such a pattern is well-suited for circular mirrors requiring symmetrical shape correction. A honeycomb layout has also been used, notably when decentralized control is required. In this case, the actuators are all identical and arranged in a hexagonal tessellation [18]. Finally, a lattice of unidirectional actuators [12,19] has been chosen for rib-stiffened deformable mirrors and ultrathin membrane mirrors.

In some applications the optical pupil diameter is not required to match the full diameter of the mirror, and hence the edge of the mirror can be excluded if the accuracy of the shape correction deteriorates near the edges. Hence, for such applications the figure of the mirror near the edges is not critical. However, in a segmented primary mirror, ideally the full surface of each segment needs to be available, and hence achieving an accurate shape near the edges of the mirror segments is important. This requirement, not adequately addressed by existing designs for deformable mirrors, and the need to minimize the number of actuators needed to correct a dominant aberration mode, were the main motivation for the study presented in this paper.

The paper is arranged as follows: Section 2 presents an actuation pattern optimization method; Section 3 describes an application of this method to the correction of astigmatism aberrations; Section 4 considers the effects of manufacturing constraints and their impact on the achievable accuracy; Section 5 presents an experimental validation of the proposed method; and Section 6 concludes the paper.

## 2. OPTIMIZATION OF ACTUATORS

Optical aberrations are described by Zernike polynomials [20], which are defined by the radial and azimuthal orders, $n$ and $m$. Their shapes and the notation used throughout this paper are presented in Fig. 3.

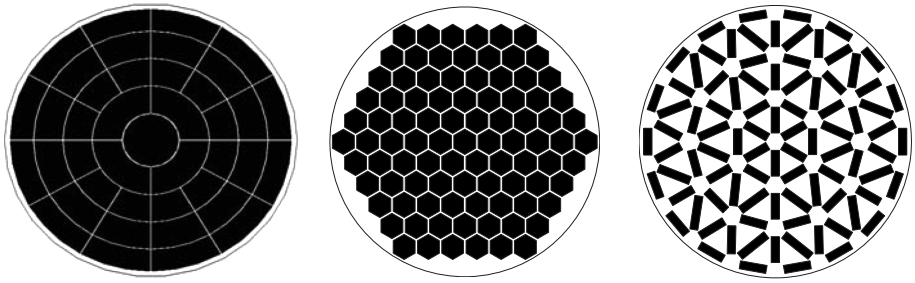


**Fig. 2.** Classical layouts of electrodes in surface-parallel actuated mirrors: (a) keystone, (b) honeycomb, and (c) lattice.

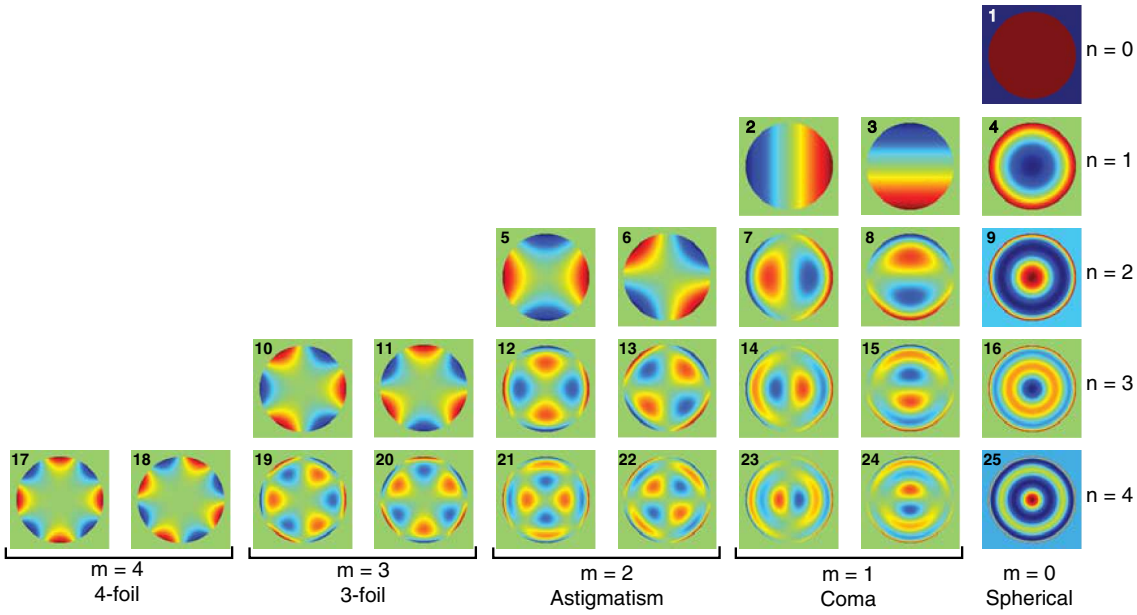


**Fig. 3.** First 25 Zernike polynomials.

The deformable mirror concept shown in Fig. 1, in which the active layer covers the whole (back) surface of the mirror, can easily accommodate any given set of correction requirements as the shapes of the individual electrodes can be modified without any impact on the other layers of the mirror. Note that it is also possible to leave some areas passive, i.e., without electrodes.

The problem of designing electrode patterns that target the correction of some specific error modes can be approached in several different ways. For example, one could consider patterns of general topology and vary the shape of the electrodes with a numerical optimizer that finds the design that provides the best performance. Alternately, one could use existing knowledge about the dominant error modes that are associated with a particular mirror concept and construction technique to develop specific types of electrode patterns that are well-suited to the correction of the dominant aberration modes. The latter approach is adopted in the present study.

### A. Actuator Geometry

As an initial step, consider the problem of designing an actuator pattern to correct for a particular error mode in a circular mirror. The most direct approach is to use a single electrode, whose shape and position are optimized with the aid of a finite-element model of the mirror and the actuator. The model is used by an optimization algorithm to predict the performance of a series of trial designs of the actuator until the pattern that produces the best possible correction is obtained. Assuming the actuator to have a singly connected shape, it can be defined in polar coordinates $(r, \theta)$ by a set of control points equally spaced in the angular direction, see Fig. 4(a). The radial positions of these points are obtained from the optimization.

If the error mode is symmetric, then the shape of the electrode must also have the same type of symmetry. The error modes considered in the present study have azimuthal order $m \geq 2$ and radial order $n \geq 2$, see Fig. 3. Hence, the actuator is defined on a sector that subtends an angle $\pi/m$. The full geometry of the actuator is obtained by reflecting the shape in the initial sector across a radial line along the edge, and then repeating this pattern through $m - 1$ rotations. Therefore, the complete pattern has $m$-fold symmetry.

The case $m = 1$, $n \geq 2$ can also be corrected, but the approach is somewhat different and will be discussed separately, at the end of this section.

A single electrode system tends to induce a curvature mode [21], hence generating a large amount of focus aberration, but this unwanted effect can be countered by the use of a second actuator. The simplest way of doing this is by introducing a second active layer stacked on the substrate. Since an axisymmetric actuator would be very effective in generating focus changes, the second actuator could have a circular shape covering the entire mirror, see Fig. 4(b). However, multi-layer actuators are technologically more complex than single-layer actuators and, furthermore, increasing the overall thickness of the mirror stack has the effect of decreasing the available dynamic correction range.

Another approach uses a configuration that will be called a *twin actuator*, consisting of two electrodes with identical shape and within the same active layer, but rotated through $\pi/m$ and actuated by applying equal and opposite voltages. The focus change induced by the first actuator is then directly suppressed by the focus change introduced by the second actuator. The specific rotation angle of $\pi/m$ ensures that the correction mode generated by the second actuator has the same orientation as that generated by the first actuator. Note that this twin-actuator configuration provides double the correction amplitude of each single actuator when equal and opposite voltages are applied to the two electrodes.

The twin actuator is built on the same piezoelectric layer, and the intersection between the two electrodes defines several

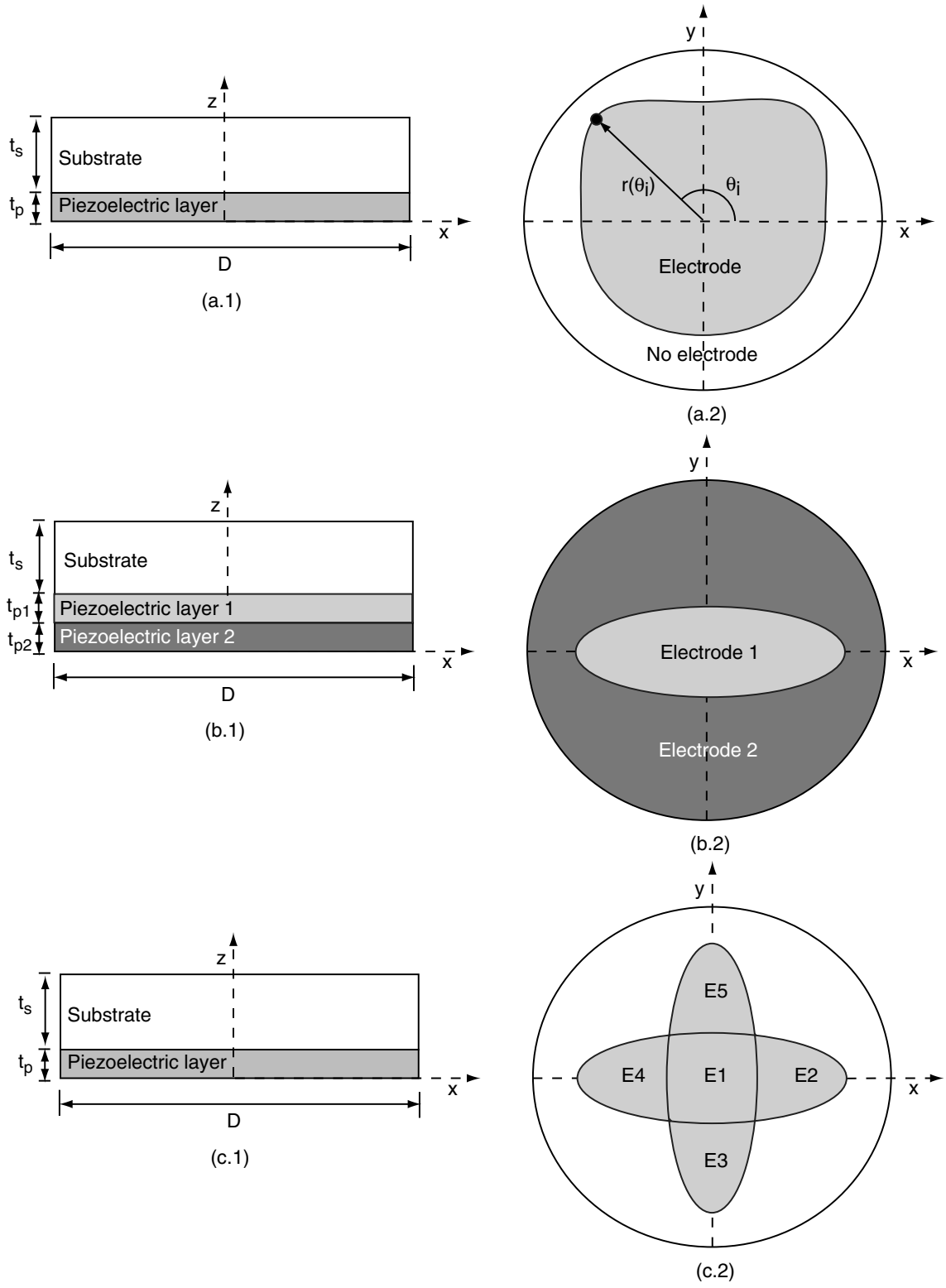


**Fig. 4.** Piezoelectric layer concepts. (a) Definition of electrode shape for single-actuator optimization. (b) Two actuators in separate layers, electrode 1 is shaped and electrode 2 covers the whole substrate. (c) Twin-actuator concept, the intersection of two basic electrodes defines 5 separate actuation zones.

separate *actuation zones*. The example in Fig. 4(c) has five actuation zones, labeled $E_1, \ldots, E_5$. Of course, in addition to applying only positive and negative voltages of the same amplitude to these electrodes, there is also the option of applying a different voltage to each electrode. Hence, it possible to correct for a range of shape errors, in addition to the basic error mode considered when originally designing the shape of the electrode.

The twin-actuator system consisting of several separate actuation zones, which was conceived as a solution to the problem of correcting a single, dominant error mode, is the basis of a more general actuator geometry that will be described next.

The general idea is to consider a set of *nested twin actuators*, each targeted to the correction of a specific error mode. The outermost twin actuator is defined by its contour $r_1(\theta)$, which is obtained from an optimization study based on a finite-element analysis that evaluates the sensitivity of the shape correction to changes in $r_1(\theta)$. The second twin actuator lies inside the first and has the same orientation; it is defined by the contour $r_2(\theta)$ which is obtained from a further optimization study. Smaller twin actuators can be nested inside the first two. Finally, the full set of twin actuators is rotated through $\pi/m$ to generate a second set that complements the first set. The purpose of the second set of actuators is to allow the correction of error modes with arbitrary orientation.

The twin-actuator geometry for the case $m = 1$, $n \geq 2$ (coma) requires a twin actuator whose basic shape is defined over a sector that subtends an angle of $\pi$. Then, this shape is reflected across a mirror line to obtain the complete shape of the first actuator, and a rotation through $\pi$ generates the twin actuator which, as before, is actuated with a voltage opposite to the first actuator.

### B. Mirror Shape Changes

Consider a mirror of diameter $D$, with substrate and piezoelectric layers, respectively, of uniform thickness $t_s$ and $t_p$. The piezoelectric layer covers the whole of the substrate, but is conceptually divided into two parts, an active part covered by the electrode and the remaining passive part. Applying an electric field to the active part induces a mismatch strain between the substrate and the piezoelectric layer, causing the mirror to bend. The deformation of the mirror is predicted by a finite element analysis in which the mirror is modeled as a thin shell with the finite element package Abaqus Standard [11,22].

The mirror model is constructed using thermoelastic thin shell elements, S4T, that are defined to have a composite stack lay-up: the substrate and active layers are modeled by defining two sections within the shell. Thermally induced strains are used to simulate the piezoelectric strains, hence a temperature field is applied as a substitute for the electric field and the thermal expansion coefficient substitutes for the $d_{31}$ coefficient of the piezoelectric material. The thermal expansion coefficient is scaled so that a temperature variation of 1 K is equivalent to the application of 1 V across the faces of the piezoelectric layer. Apart from out-of-plane effects, which are of no importance in the present case, this analysis is equivalent to modeling linearized piezoelectricity directly, but the present approach has the advantage of using standard finite elements.

A preliminary estimate of the correction curvature, $\kappa$, can be obtained by considering the deformation of a circular substrate due to stress applied by a piezoelectric layer covering the entire substrate. In this case, the curvature can be estimated from the biaxial moduli, $M$, of the substrate (denoted by the subscript $s$) and the piezoelectric layer (subscript $p$), defined as $M = \frac{E}{1-\nu}$, where $E$ is the Young's modulus and $\nu$ the Poisson's ratio [23]:

$$\kappa = 6 d_{31} \frac{V_l}{t_p} \frac{\frac{t_p}{t_s^2}\frac{M_p}{M_s}\left(1+\frac{t_p}{t_s}\right)}{1+\left(4\frac{t_p}{t_s}+6\frac{t_p^2}{t_s^2}+4\frac{t_p^3}{t_s^3}\right)\frac{M_p}{M_s}+\frac{t_p^4}{t_s^4}\frac{M_p^2}{M_s^2}}, \quad (1)$$

where $V_l$ is the voltage limit and hence $V_l/t_p$ is the maximum electric field that can be applied to the piezoelectric layer without depoling.

Given the required curvature correction, Eq. (1) can be used to estimate the thickness of the piezoelectric layer, if all other parameters are known.

Detailed estimates of the deformed shape of the mirror can be obtained from the finite element model, for any chosen shape of the active part of the piezoelectric layer and for the selected mechanical properties and thickness of both substrate and piezoelectric layers. The optimal shape of the electrode can be determined by defining a suitable objective function, $f$, and by optimizing its value through changes in the shape of the electrode. This optimization can be carried out by coupling the finite element analysis with a minimizer suitable for nonconvex problems. An algorithm that performs a global search of the design space is the covariance matrix adaptation evolution strategy algorithm (CMAES) [24].

### C. Problem Formulation

The wavefront error is defined by the initial error, $P$. It should be noted that the wavefront error, which is equal to two times the surface error, is the only error measure quoted throughout the paper. As a first case, assume that $P$ has a single Zernike component with radial order $n \geq 2$ (because piston, tip, and tilt errors can be corrected by means of rigid-body actuators):

$$P = a_i Z_i, \quad (2)$$

where $Z_i$ is the Zernike mode of the error and $a_i$ its amplitude.

Any trial design of the actuator pattern is characterized by its influence matrix, $F$, which contains the wavefront maps induced by a unit command on each actuator [25]. Projecting the initial error onto the column space of $F$ gives the set of voltage commands

$$V = F^+ P, \quad (3)$$

where $F^+$ is the generalized inverse of $F$. Then, the actual wavefront correction is

$$P_c = FV \quad (4)$$

and the residual error is

$$R = P - P_c. \quad (5)$$

The performance of a trial actuator design is then characterized by two quantities:

- its correctability, $c_i$, given by the ratio between the root-mean-square (RMS) amplitude of the wavefront error before and after correction:

$$c_i = \frac{\|P\|_{\text{rms}}}{\|R\|_{\text{rms}}}; \tag{6}$$

• its stroke, $s_i$, given by the maximum amplitude of the mode that can be corrected without saturating any actuators. $s_i$ depends on the voltage limit, $V_l$, and the largest voltage command obtained from Eq. (3), $\max(V)$:

$$s_i = \frac{V_l}{\max(V)} a_i. \tag{7}$$

It should be noted that the above definition of stroke uses an estimation of the actuator voltages that does not account for any voltage constraints. This approach leads to severe underestimates of the capability of a deformable mirror because, although the saturation of a few actuators leads to reduced correctability, most mirror designs are still able to provide significant corrections beyond the point at which some actuators have saturated. A more detailed discussion of this issue is provided in Section 3.B.

In order to maximize both correctability and stroke for mode $i$, the following multi-objective function $f$ is defined as

$$f = \lambda_1 c_i + \lambda_2 s_i, \tag{8}$$

where $\lambda_1$ and $\lambda_2$ are weights allocated to the two quantities, depending on specific correction requirements.

The above problem formulation can be readily generalized to wavefront errors including several Zernike modes, i.e., Eq. (2) is replaced by

$$P = \sum_i (a_i Z_i). \tag{9}$$

The *overall correctability* and *overall stroke* are then defined as

$$\overline{c} = \sum_i \beta_i c_i, \overline{s} = \sum_i \beta_i s_i, \tag{10}$$

where $\beta_i$ is the weight allocated to Zernike mode $i$, depending on the correction requirements, and the summation is extended to the range of modes of interest.

Third-order aberrations (i.e., the five aberration modes in the row $n = 2$ of Fig. 3) are generally the most important because they correspond to the first errors that appear in an optical system [26], hence a weight of 1 was allocated in the present study. Fifth-order aberrations (shown in the row $n = 3$ of Fig. 3) had a weight of 0.1 and seventh-order aberrations (shown in the row $n = 4$ of Fig. 3) had a weight of 0.01. These values were chosen on the basis of manufacturing, thermal deformation, and misalignment shape errors that are typically encountered in active optics applications. Different values would be chosen for applications such as adaptive optics. Note that a weight of zero was allocated to piston, tip, tilt, and focus aberrations: these modes are generally corrected by means of a separate system [27].

## 3. ASTIGMATISM-BASED ACTUATOR PATTERNS

Third-order astigmatism is one of the most important aberration modes in an optical system: it is a significant component of the initial shape distortion of mirrors and one of the first off-axis aberrations induced by misalignment [28]. Hence, deformable mirror designs need to be particularly efficient in the correction of this mode and, because the magnitude of third-order astigmatism aberrations is often large, a significant stroke (dynamic range) is also needed. This section presents several designs of actuator patterns optimized for astigmatism correction.

While the correctability of a deformable mirror depends only on the geometry of the electrode pattern, its stroke depends also on the diameter of the mirror, as well as on the curvature that can be achieved by reaching the voltage limits of the actuators [which can be predicted with Eq. (1)].

Mirrors with a diameter of 100 mm and with the same thickness and material properties as the mirrors studied in Ref. [11] were considered. These mirrors are flat and consist of a 200 μm layer of glass ($E_s = 65$ GPa, $\nu_s = 0.2$) and a 20 μm layer of P(VDF-TrFE) ($E_p = 1.45$ GPa, $\nu_p = 0.34$). The limit voltage was set at 500 V.

The main reason for studying flat mirrors is that they can be built more easily, making it cheaper to test prototypes of the proposed solutions. It should be noted that, the results obtained in the present study are in fact applicable also to mirrors that are slightly curved. For example, for a radius of curvature of 2 m the RMS difference between the influence functions for a flat and a curved mirror with the same actuator design, is of the order of 0.7% the amplitude of the influence function for the flat mirror.

### A. Basic Set of Actuators

Third-order astigmatism has two planes of mirror symmetry, see Fig. 3, and hence only a quarter of the basic electrode shape needs to be determined. The problem of finding the shape of one-quarter of the basic electrode was formulated as described in Section 2.C, biasing the solution toward higher correctability and lower stroke, by assigning $\lambda_1 = 10$ and $\lambda_2 = 1$ in the objective function of Eq. (8). The reason for assigning a lower weight to the stroke is that, as noted in Section 2.C, the stroke defined in Eq. (7) provides an underestimate of the true correction amplitude of which a mirror is capable.

The results of the shape optimization for a single electrode, defined by the values of $r(\theta)$ at 6 points located in one quadrant, are presented in Fig. 5(a). The optimal shape for a single actuator is the bow-tie shape in Fig. 5(a1) and, for a third-order astigmatism aberration with RMS amplitude of 1 μm, the best possible correction is close to a cylindrical deformation, Fig. 5(a2). The residual total wavefront RMS error is 1.587 μm, Fig. 5(a3), which is reduced to 0.378 μm after removal of the focus aberration. The correctabilty and stroke [obtained from Eqs. (6) and (7)] of this system are $c_5 = 0.6$ and $s_5 = 1.5$ μm.

A twin actuator was also designed, as explained in Section 2.A. The basic electrode shape was obtained, as before, by computing 6 points located in one quadrant. It resembles an ellipse and for simplicity it will be described by the lengths of the horizontal and vertical semiaxes. Overall, the twin-electrode pattern consists of a large central part defined by the intersection of two ellipses, labeled E1 in Fig. 4(c2), subjected to a voltage of zero, surrounded by four crescent-shaped regions labeled, E2 to E5, alternately subjected to positive and negative voltages of equal magnitude. The size of the zones E2 to E5

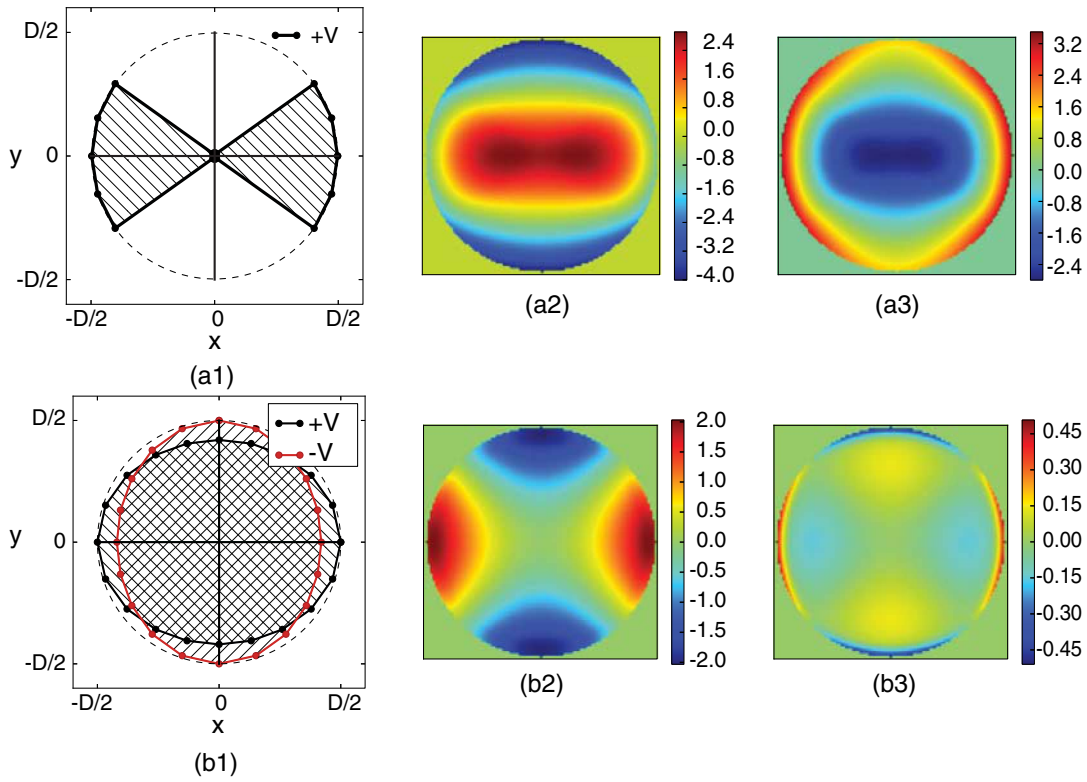


**Fig. 5.** Optimized electrode shapes and system performance for the correction of 1 μm RMS of astigmatism. (a1) Single-actuator configuration. (a2) Correction, including focus aberration (1.875 μm RMS). (a3) Residual wavefront error (1.587 μm RMS). (b1) Twin-actuator configuration. (b2) Correction (1.002 μm RMS). (b3) Residual wavefront error (0.104 μm RMS). (Units: μm.)

depends on the weights given to stroke and correctability when defining the optimization function, but the overall pattern is general.

The optimized configuration and performance of this twin-actuator system are presented in Fig. 5(b). Overall, this design is able to correct third-order astigmatism with a correctability of 10 and a stroke of 3 μm. Compared to the single actuator system performance, the correctability has increased by a factor of 17 and the stroke by a factor of 2.

Varying the ratio between the length of the major axis (which is equal to the mirror diameter) and the length of the minor axis of the two ellipses controls the system performance. The performance trends have been studied numerically, assuming the actuators to be exactly of elliptical shape to simplify the parametrization of their geometry; the results are shown in Fig. 6. Note that a configuration with an axis length ratio close to 1, which has narrow actuation zones E2 to E5, is the most efficient in generating astigmatism correction but has limited stroke. On the other hand, a configuration with a smaller axis length ratio leads to larger edge actuators and significantly improves the stroke, but at the expense of a lower correctability.

Figure 6 also shows that reducing the ratio between the optical pupil diameter and the mirror diameter has a significant impact. Because the residual error is largest near the edge of the mirror, choosing a smaller pupil leads to a better correctability.

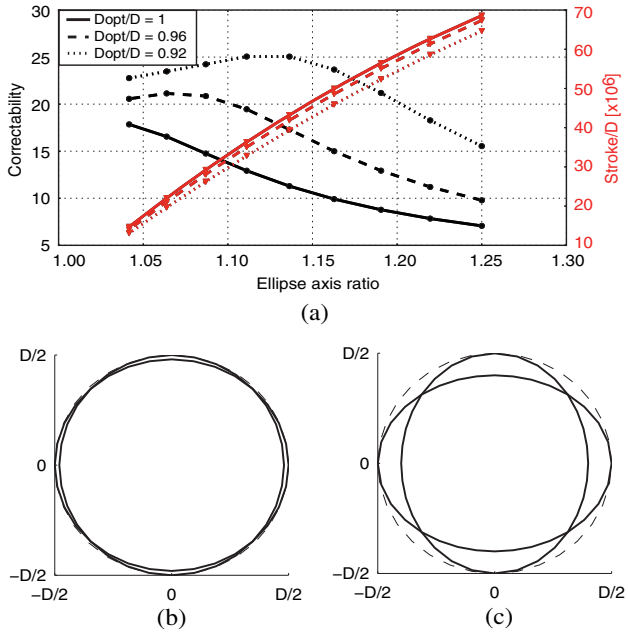


**Fig. 6.** (a) Evolution of correctability and stroke with ellipse and pupil dimensions, for third-order astigmatism correction provided by system in Fig. 5(b1). Actuator patterns for ellipse axis ratios of (b) 1.04 and (c) 1.25.

### B. Additional Actuators

The twin-actuator system presented in the previous section provides an efficient solution for the correction of third-order astigmatism, leaving a residual wavefront error mainly composed of higher-order astigmatism, see Fig. 5(b3). Additional, internal actuators are introduced to compensate for this residual error, as well as providing a capability to correct for other aberration types. This section deals with the design of the internal actuators to further improve the correction of third-order astigmatism, whereas the correction of other error modes is discussed in the following section.

As a first modification to the basic twin-actuator system, a second set of twin actuators is nested inside the previously defined set, Fig. 7(a1). It consists of two orthogonal electrodes whose common shape is determined by solving an optimization problem in which both correctability and stroke for third-order astigmatism correction are considered. For each optimization trial, the different electrode commands are determined from Eq. (3) and the correctability and stroke are computed from Eqs. (6) and (7). The objective function, Eq. (8), is defined with the same weights as in Section 3.A, $\lambda_1 = 10$ and $\lambda_2 = 1$.

Figure 7(a) presents the results for a system consisting of two sets of twin actuators. In the figure, note that the shape of the inner electrodes is also closely approximated by an ellipse; the major axis of the inner ellipse matches the minor axis of the outer ellipse, hence leading to a maximum area of active material. The minor axis drives the achievable stroke and correctability. The ratios between the major and minor axes for the outer and inner sets of ellipses are 1.19 and 1.23, respectively. The similarity between the internal and external electrode

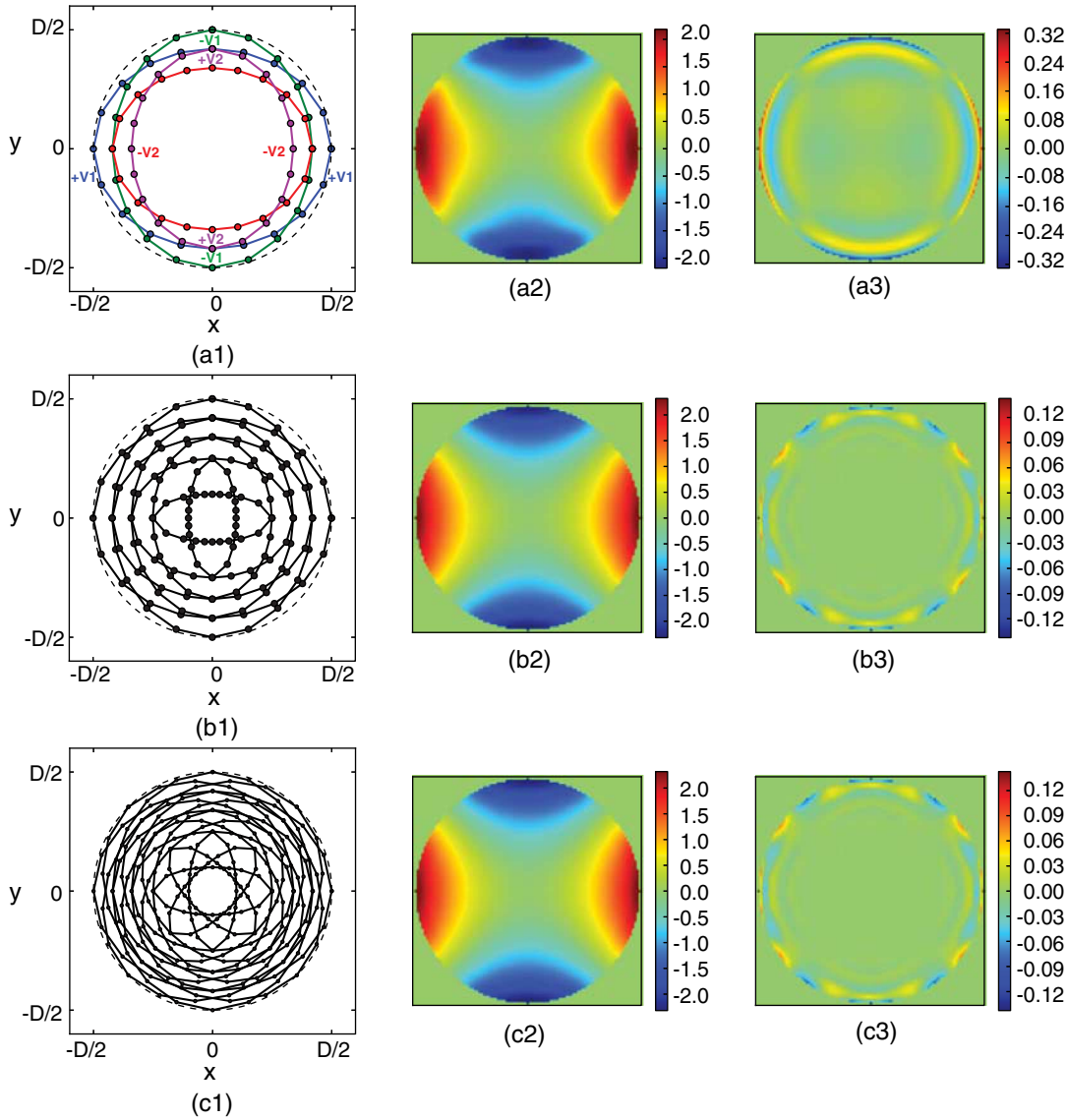


**Fig. 7.** Optimized electrode patterns and system performance for the correction of 1 μm RMS of astigmatism. (a1) Two sets of twin actuators resulting in 13 actuation zones. (a2) Correction (0.993 μm RMS). (a3) Residual wavefront error (0.053 μm RMS). (b1) Four sets of twin actuators resulting in 29 actuation zones. (b2) Corrected wavefront (0.993 μm RMS). (b3) Residual wavefront error (0.050 μm RMS). (c1) Four sets of twin actuators plus four additional sets at 45° resulting in 129 actuation zones. (c2) Correction (0.994 μm RMS). (c3) Residual wavefront error (0.014 μm RMS). (Units: μm.)

patterns can be explained by the fact that higher-order astigmatism aberration corresponds to third-order astigmatism on a smaller circle. Note that the addition of the inner twin actuator has increased the correctability by a factor of 2.

Additional sets of twin actuators can be added inside these two sets, to further improve the mirror performance. The outcome is an actuator system with several nested actuation zones. For example, Fig. 7(b1) shows an actuation system consisting of four nested rings of orthogonal ellipses. The optimized ellipses axes ratios for the external, 2nd, 3rd, and 4th set are, respectively, 1.19, 1.23, 1.36, and 2.5.

A more general pattern that can correct for astigmatism in any direction can be obtained by rotating through 45° the above sets of actuators and then defining smaller actuators from the intersections between the original and rotated actuators. The overall electrode pattern consists of 129 independent actuation zones, providing a highly efficient correction of astigmatism in both $x$ and $y$ directions. The correctability provided by this pattern is improved by a factor of almost 10 compared to the configuration in Fig. 7(a1).

An important issue that arises when considering actuator patterns with smaller and smaller features is that, due to the small volume of active material associated with tiny actuators, these actuators tend to saturate much earlier than larger ones. Hence, the stroke $s_i$ defined in Eq. (7), which assumes a hard stop at first saturation, becomes a rather misleading performance criterion, as it neglects a large residual correction capability. For example, for third-order astigmatism correction of the actuator design shown in Fig. 7(c1) the voltage command for the outermost, tiny actuators is 100 times larger than for the innermost actuators.

Therefore, although the stroke continues to be a useful indicator of performance, a more effective representation of the true correction capability of a mirror design is the *variation in correctability with error amplitude*, which can be computed with a constrained least squares algorithm [29]. For the example design in Fig. 7(c1), a voltage limit of ±500 V was imposed and the evolution of the amplitude of the residual error (output) with the initial error amplitude (input) was computed. The results are presented in Fig. 8. For small inputs there are no saturated actuators and hence the output varies linearly with the input; the slope of the output/input graph corresponds to the reciprocal of the system correctability, which has an initial value of 71. When some of the tiny edge actuators reach saturation, all further voltage increments are subject to the constraint that the voltage in the saturated actuators can only remain constant or be decreased. Hence, at this point the correction performance is slightly degraded as the slope of the output/input graph increases. However, the overall performance remains quite good, with a correctability of ~60, as long as the only saturated actuators are the small ones, which have no significant impact. For input amplitudes of around 1.3 μm RMS, the edge crescent actuators also begin to reach saturation and from this point there is a further decrease in correctability, to ~40.

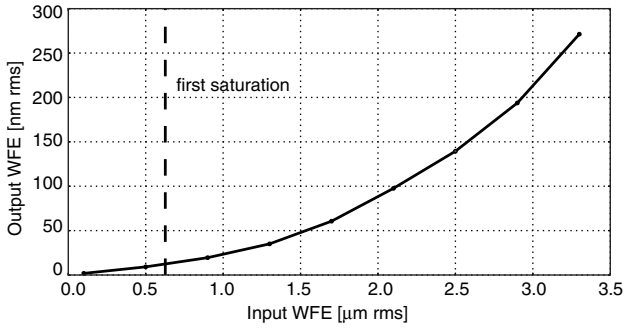


**Fig. 8.** Performance of the 129-actuator system: evolution of the residual wavefront error with the amplitude of third-order astigmatism (considering a pupil of 98% of the total mirror diameter).

In conclusion, it has been shown in this section that a basic set of four edge actuation zones allows a coarse correction capability that is gradually improved by adding internal actuators. The overall system can efficiently correct third-order astigmatism, even when some actuators become saturated, providing a good correctability and a significant dynamic range. Other types of aberrations are considered in the next section.

### C. Correction of Other Zernike Modes

In addition to providing an efficient correction of third-order astigmatism, the 129-actuator layout shown in Fig. 7(c1) can be used to correct other types of aberrations. Its computed correctability and stroke for each of the first 25 Zernike modes are presented in Fig. 9(a). The overall correctability and stroke, computed from Eq. (10) with $\beta_i = 0$ for $i = 1, \ldots, 4$, $\beta_i = 1$ for $i = 5, \ldots, 9$, $\beta_i = 0.1$ for $i = 10, \ldots, 16$, and $\beta_i = 0.01$ for $i = 17, \ldots, 25$, are presented in Fig. 9(b).

Two different ratios of optical pupil diameter to overall mirror diameter have been considered; note that the correctability

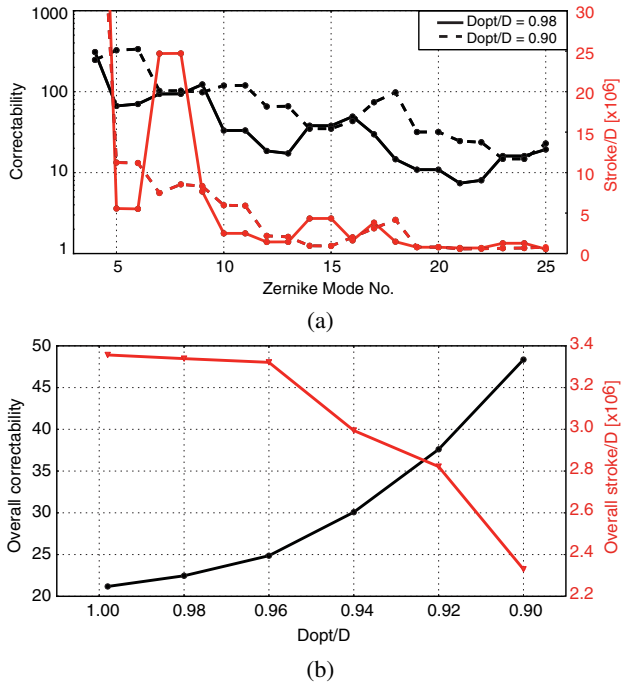


**Fig. 9.** Performance of the 129-actuator system. (a) Correctability and stroke of first 25 Zernike polynomials for two pupil sizes. (b) Evolution of the overall correctability and stroke [defined in Eq. (10)] with pupil size.

increases significantly with even relatively small reductions in pupil size.

In Fig. 9(a) the evolution of the correctability with Zernike modes of increasing order is very satisfactory; for a pupil diameter of 98 mm the correctability is higher than 10 for all but two modes. For a pupil diameter of 90 mm the correctability is higher than 30 for the first 20 modes. The stroke values, also plotted in Fig. 9(a), are relatively low for the reasons already discussed in Section 3.B. However, a more detailed examination of the variation in correctability with error amplitude, accounting for actuator saturation by means of a constrained least squares algorithm, shows that beyond first saturation the reduction in correctability is gradual and follows the same trend as in Fig. 8 also for other types of aberrations.

In conclusion, the actuator configuration in Fig. 7(c1), although optimized for third-order astigmatism generation, is in fact able to efficiently correct the first 25 Zernike polynomials, making this design suitable for many potential applications.

## 4. MANUFACTURING CONSTRAINTS

The 129-actuator mirror shown in Fig. 7(c1) is an ideal design that has been optimized for astigmatism correction and has been shown to correct efficiently also other Zernike modes. However, there are some practical limitations on the electrode pattern when one considers the physical implementation of this design.

First, each electrode has to be large enough that a physical connection to the voltage controller can be built. The actual limit depends on the fabrication process; in the present study a minimum contact area of 1 mm × 1 mm was assumed. Second, the electrodes must be physically separated; the separation distance depends on the fabrication process as well as the presence (or not) of an insulating coating on the electrode. In the present study a minimum interelectrode distance of 0.5 mm was assumed. Finally, to avoid shorting across the edges of the mirror, the electrodes cannot extend to the edge of the mirror, hence a clear annulus with a radial width of 1.5 mm minimum was assumed.

The reduction in performance of the mirror due to these constraints is discussed in the following subsections.

### A. From Ideal to Feasible Patterns

The finite element model of the optimized mirror design was modified to analyze two configurations incorporating the manufacturing constraints described above. The first configuration had gaps of 0.5 mm between the actuators and a 1.5 mm wide clear annulus around the edge. The alternative configuration had 1 mm gaps between the actuators and a 2 mm clear annulus around the edge. It can be seen in Fig. 10 that even the introduction of the smaller clear annulus has the effect of removing the eight tiny electrodes near the edge, hence reducing the number of actuators to 121. The computed performance of each pattern is presented in Fig. 11(a), in terms of correctability for each of the first 25 Zernike modes. Note that astigmatism and trefoil correction are the most affected by the removal of the eight edge actuators.

It is interesting to analyze the different contributions to the loss of performance of the ideal pattern. They are presented in Fig. 11(b) in terms of overall correctability and overall stroke for the ideal configuration with 129 actuators, for the configuration with only 121 actuators with no gaps, and for the 121-actuator configurations with small and large gaps. The figure shows that the removal of the eight tiny edge actuators leads to a 22% reduction in correctability together with a gain in stroke of 25% (because the edge actuators were the first to saturate). The small gaps between the electrodes lead to a further 10% reduction in overall correctability, and the larger gaps to a 30% reduction. The stroke is, respectively, decreased by 30% and 50%, compared to the 121 electrodes pattern without gaps.

In conclusion, it has been shown that the introduction of interactuator gaps affects all modes roughly in the same way, whereas introducing a clear edge affects mostly the modes involving edge actuation. The latter effect can be mitigated by a reduction in the pupil diameter, as outlined in Fig. 9(b).

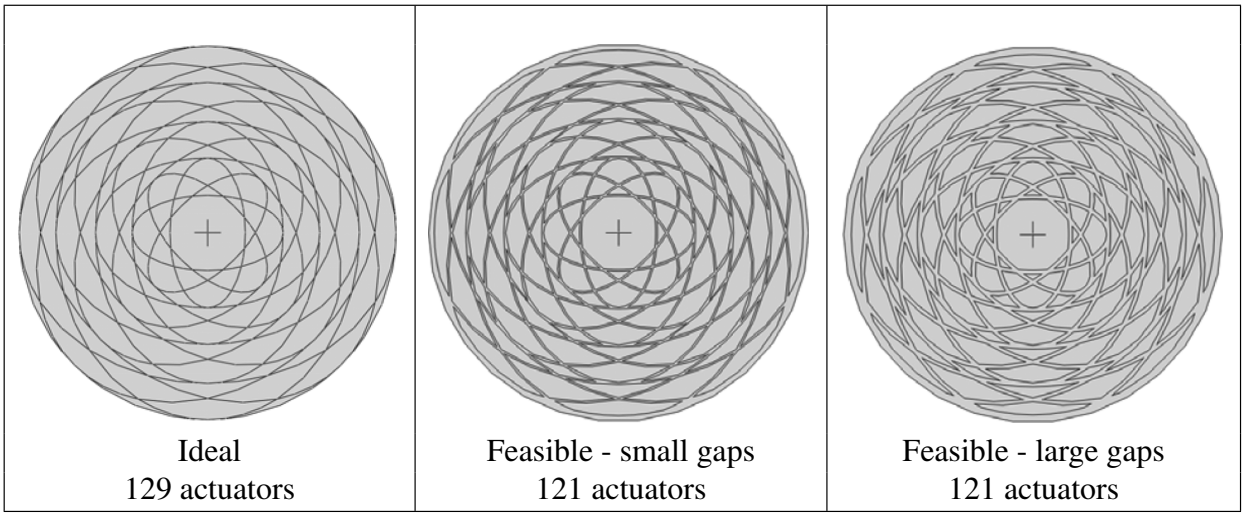


**Fig. 10.** Effects of manufacturing constraints; the clear edges induce the loss of 8 actuators and the interactuator distance induces a loss of active material.

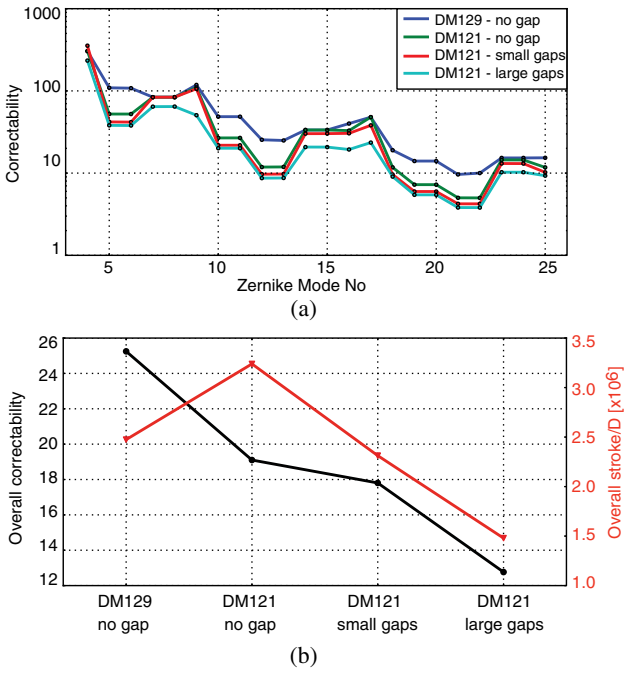


**Fig. 11.** Performance comparison between ideal and feasible patterns, considering a pupil of 97% of the total mirror diameter. (a) Correctability of the first 25 Zernike modes. (b) Overall correctability and stroke, as defined in Eq. (10), for different mirror designs.

### B. Simplified Actuator Patterns

It is also interesting to explore the trade-off between performance and total number of independent actuation channels. Hence, starting from the 121-actuator optimized pattern with no gaps, the number of actuators was reduced by grouping together neighboring actuators and the performance of the simplified mirror designs obtained in this way was computed with the finite element model. Alternative groupings of the actuators were also considered and the configurations with the best mean performance were selected and used to develop further simplified configurations. The four axes of symmetry of the initial pattern were maintained throughout this process and the edge actuators were maintained as they are essential for third-order astigmatism correction.

This evolution of the actuator pattern from 121 to 41 actuators is presented in Fig. 12 and the mean correctability and stroke of the simplified designs are presented in Fig. 13, for a pupil diameter of 97% of the total diameter. As already seen in Fig. 9(b), an improved performance is obtained for a smaller pupil size.

The performance of the mirror decreases by a relatively small amount when the 121 actuators are reduced to 57, but the decrease is comparatively much larger when going from 57 to 41 actuators. For example, the overall correctability is initially decreased by only 20% when the number of actuators is more than halved, but it is then decreased by 20% when a further 25% of the actuators are removed.

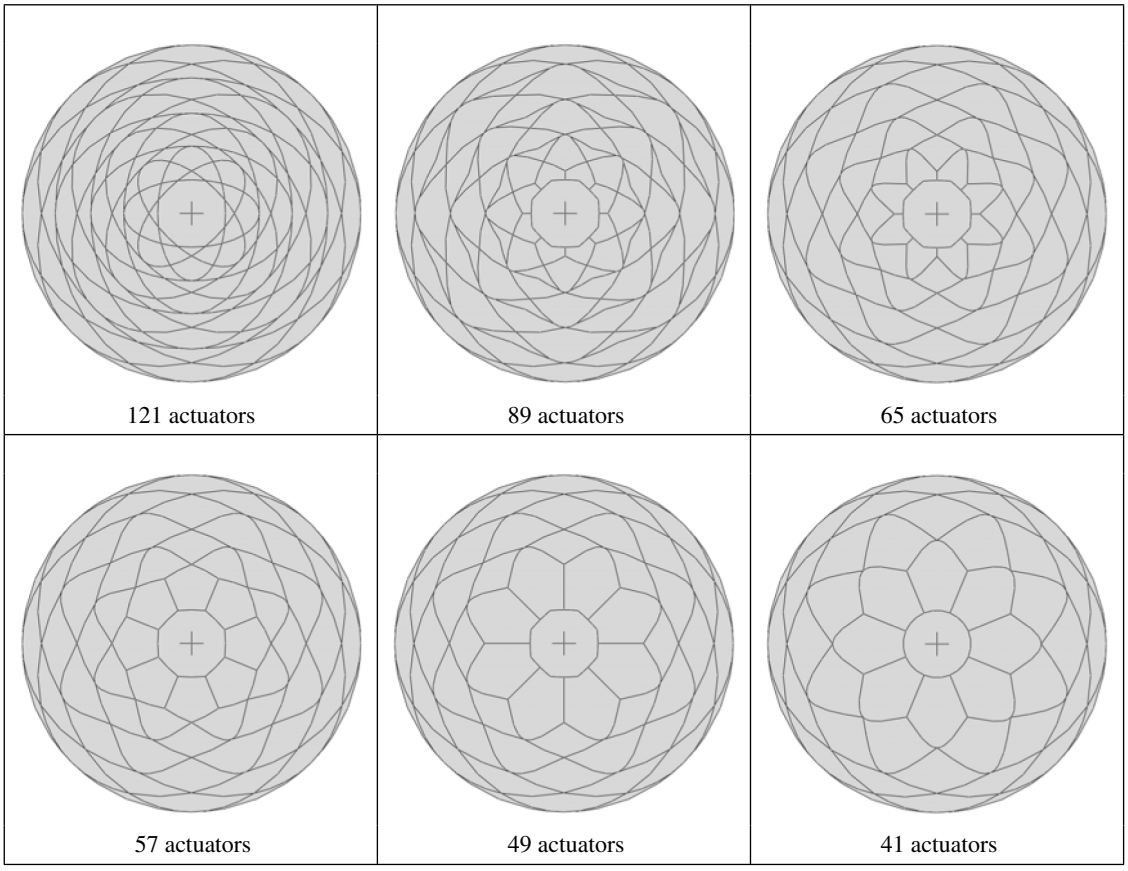


**Fig. 12.** Designs with decreasing numbers of actuators.

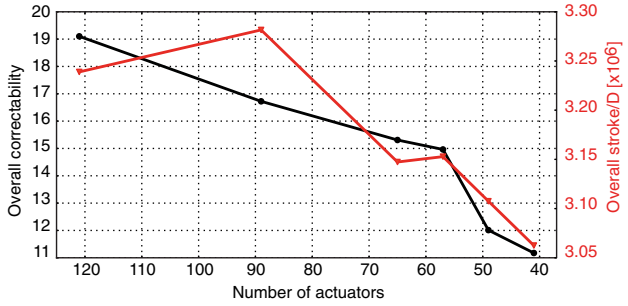


**Fig. 13.** Overall performance of actuator designs presented in Fig. 12, considering a pupil of 97% of the total mirror diameter.

### C. Comparison to Classical Patterns

A comparison between the performance of the optimized actuator pattern with 41 actuators, shown in Fig. 12, and the three classical patterns shown in Fig. 2 was carried out. For this study, the detailed geometry of each pattern was modified as explained in Section 4.A, by incorporating 0.5 mm interactuator gaps and a 1.5 mm wide clear annulus around the edge. The performance of each design was computed with a finite element model analogous to that described in Section 2.C. The results are presented in Fig. 14.

Figure 14(a) shows plots of correctability for the first 25 Zernike modes. It can be seen that the optimized design provides by far the best correctability for third- and fourth-order astigmatism (modes 5, 6 and 12, 13). It has the best or equal best correctability for 14 modes and is within 50% of the best correctability for three more modes. The keystone design with 41 actuators shown in Fig. 2(a) is significantly better for modes 9, 17, 23, and 24. Note that the honeycomb design with 91 actuators shown in Fig. 2(b) and the lattice design with 90 actuators shown in Fig. 2(c) have worse performance than the optimized design for all modes.

Figure 14(b) shows plots of the residual wavefront error (output) for increasing amplitudes of a third-order astigmatism aberration. The initial slopes of the four input–output curves correspond to the correctability values for mode 5. Hence, as already seen in Fig. 14(a), the optimized actuator pattern has the lowest residual outputs and the lattice design is the second best. The keystone design produces a nearly linear response, as it is the least affected by actuator saturation, and for input errors with amplitude greater than 2.5 μm provides the lowest residual errors.

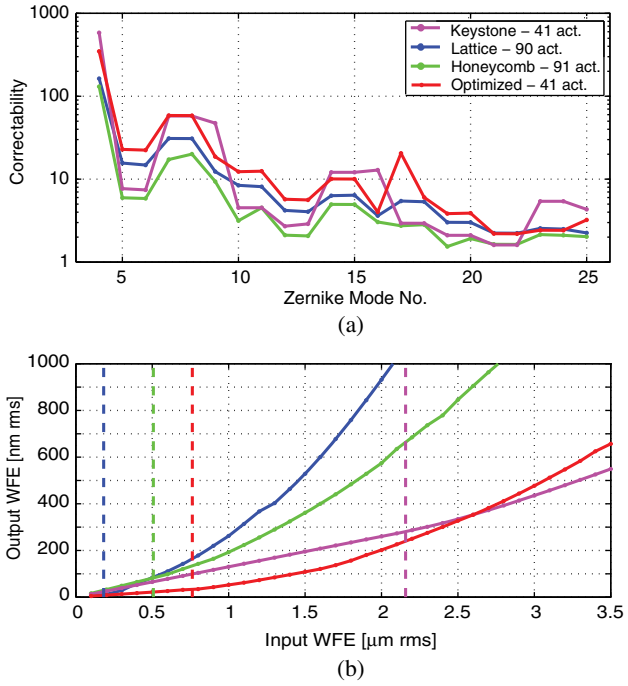


**Fig. 14.** Performance comparisons between the optimized 41-actuators pattern obtained in this paper with three classical patterns shown in Fig. 2. A pupil of 97% of the total mirror diameter has been assumed. (a) Correctability of the first 25 Zernike modes and (b) variation of the residual error for third-order astigmatism aberration of increasing amplitude.

## 5. EXPERIMENTS

### A. Mirror Design and Manufacturing

The 41-actuator mirror shown in Fig. 12 was manufactured with the techniques described in Patterson and Pellegrino [11]. The main steps of the manufacturing process were as follows:

- Coating of the front face of the polished glass substrate with reflective material and thermal balancing layer;
- Deposition of the ground layer;
- Deposition of the piezopolymer layer on the back face of the glass substrate via spin coating, and curing of the piezopolymer;
- Coating of the piezopolymer layer with a conductive film using vacuum sputtering; the electrode pattern is obtained by covering the piezopolymer layer with a shadow mask during this process;
- Poling of the piezopolymer layer by applying a high voltage;
- Annealing of the piezopolymer layer;
- Kinematic mounting of the mirror onto a printed circuit board by means of three assemblies of magnetic spheres around the edge;
- Wire bonding of the individual electrodes to the circuit board;
- Attachment of the mirror assembly to an optical bench through a gimbal that provides piston, tip and tilt adjustment.

In addition to the interactuator gaps and clear edge region discussed in Section 4, three additional clear areas at 120° spacing were created to allow for kinematic mounting of the mirror at locations near the edge. Finally, a straight edge was introduced in the electrode pattern to facilitate the alignment of the different layers.

A nominally flat mirror obtained from this process is shown in Fig. 15. This mirror has a 100 mm diameter, optical quality surface, 235 μm thick borosilicate glass substrate, and 10 μm thick P(VDF-TrFE) coating. These thicknesses are slightly different from those considered in Section 3, but its behavior is qualitatively unchanged.

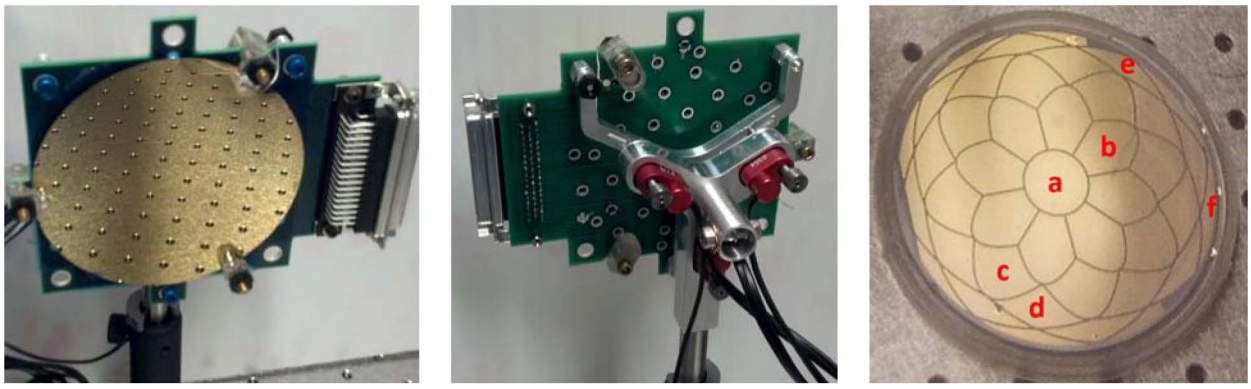


**Fig. 15.** (a) Front view of the mounted mirror showing the reflective surface and three mounting points. (b) Rear view of the mounted mirror showing electronic board and gimbal. (c) Electrode pattern with labeling of 6 unique influence functions.

### B. Testing

The influence functions of 41-actuator mirrors made with the process described in the previous section were measured on an optical testbed based around a ThorLabs WFS150-7AR Shack–Hartmann wavefront sensor conjugated with the deformable mirror. The sensor provides 39 × 31 lenslets. Figure 16 shows a diagram of the experimental setup. It consists of a 633 nm laser beam filtered with a pinhole, collimated, reflected off the deformable mirror under test, and then passed to the wavefront sensor by means of a beam splitter and lens. This arrangement was chosen so as to reimage the mirror pupil to a smaller size that fits inside the sensor aperture. The wavefront was sampled through the sensor lenslet array.

The Shack–Hartmann sensor had been calibrated by the manufacturer. A thick, flat mirror was first used to align the setup; then, the flat mirror was replaced with the deformable mirror and the Shack–Hartmann sensor was moved in the piston direction in order to zero the bulk mirror defocus and capture the image of the pupil (mirror). With this procedure, the shape measurement was relative to the closest sphere. Due to the relay lens magnification, the measurements were limited to a 100 mm by 80 mm (39 by 28 spot array) image area, and trimmed down to an 80 mm pupil diameter.

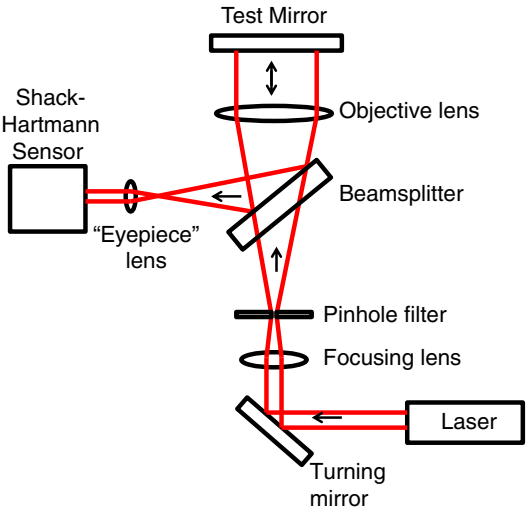


**Fig. 16.** Layout of test setup [11].

The mirror behavior was characterized through its influence functions. The influence function for each uniquely shaped electrode, see the labeling in Fig. 15(c), was measured by taking the difference between a reference measurement with all channels off, and a new measurement with a single channel turned on and set to 500 V. The local slopes of the wavefront were measured by the Shack–Hartmann sensor and from the slopes the wavefront error map was reconstructed with a zonal reconstructor, which integrates the measured slopes on the optical aperture [30]. The measurements and the predictions, obtained from a finite element model that matches the measured substrate and coating thicknesses, are shown in Fig. 17. Visually, there is a very good match between measurements and predictions for both shapes and amplitudes. This gives confidence in the modeling process and validates the design optimization work.

Based on these results, the expected performance in terms of correction of focus, astigmatism, and coma for this mirror were obtained; these performances are shown in Fig. 18. Correction is defined as $1 - 1/c_i$, with $c_i$ defined according to Eq. (6). The figure shows plots of the RMS residual error for each of the three aberrations. The linear part of each plot corresponds to the unsaturated response of the mirror, with correctability correction in excess of 99.7% for focus, 98% for coma, and 96% for astigmatism. The nonlinear part of each plot indicates the performance achievable for error amplitudes beyond the saturation limit.

As mentioned in Section 1, the mirror technology presented in this paper is targeted toward primary segmented mirrors. In this case, the mirror segments would all be made initially spherical and the actuators would be used to deform the initially spherical mirrors into an off-axis parabola. For this application, the correction of focus, astigmatism, and coma is the key to achieving an accurate off-axis shape, and hence the shape correction considered above is particularly relevant.

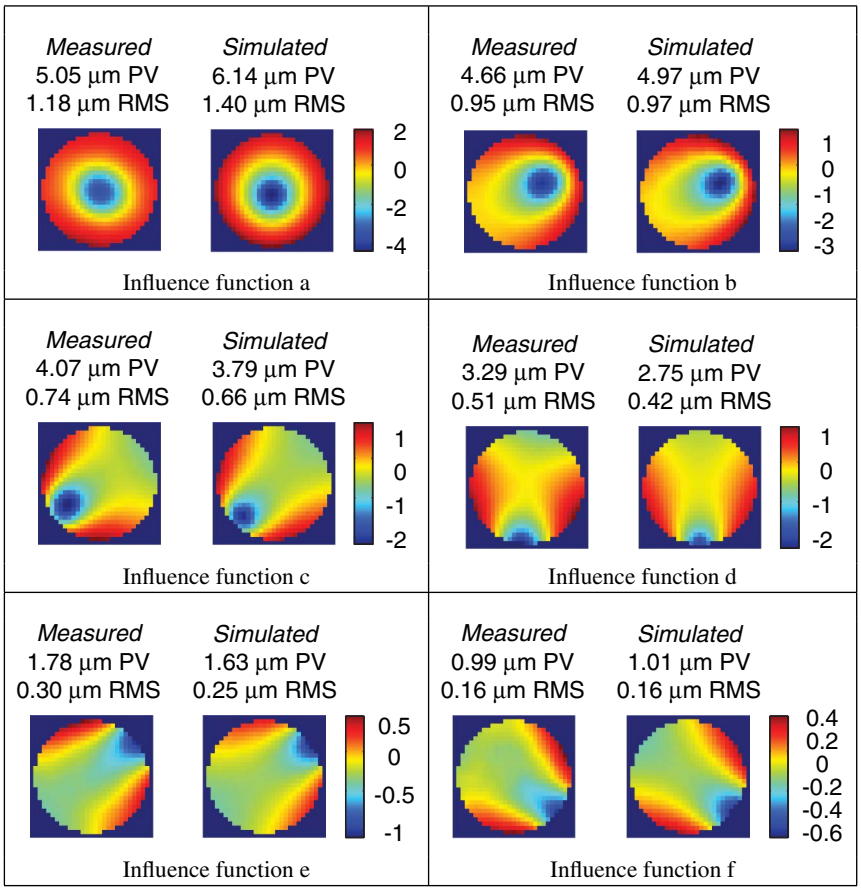


**Fig. 17.** Side-by-side comparisons of measured and simulated unique influence functions for the manufactured mirror. The 6 unique influence functions are defined in Fig. 15(c). (Units: μm.)

In connection with this type of application, it should also be noted that the 41-actuator pattern has already been adapted to hexagonal mirrors [16].

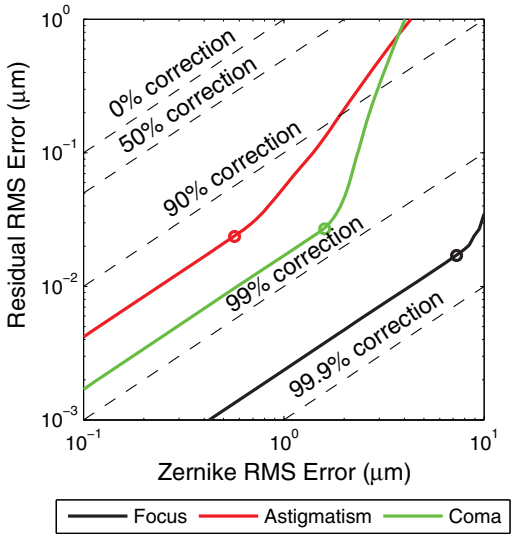


**Fig. 18.** Expected performance of the manufactured mirror for focus, astigmatism, and coma correction, considering a pupil of 97% of the total mirror diameter.

## 6. CONCLUSION

A novel actuator design and selection scheme for surface-parallel actuators for ultrathin mirrors has been presented, further developing the concept first proposed in Ref. [11] The actuation scheme consists of a pattern of electrodes printed on a continuous layer of piezoelectric material, with small separation gaps to avoid electrical shorts.

Instead of arranging the electrodes according to a simple geometric pattern, as in previous mirror designs, a set of novel shape-optimized patterns has been proposed. Each pattern fully covers, apart from the small separation gaps, the piezoelectric layer, and thus maximizes the amount of active material that is available for actuation. The proposed patterns maximize a weighted average of correctability and stroke of the mirror for a chosen number of independent actuators and for a dominant imperfection mode.

The basis for the proposed approach was the observation that the correction of a figure error that has at least two planes of mirror symmetry, and hence has azimuthal order $m \geq 2$, is optimally done with twin actuators that have the same optimized (near-elliptical, for the correction of astigmatism errors) shape but are rotated through $\pi/m$. Applying a positive voltage to the first actuator and a negative voltage to the second one has the effect of removing the axisymmetric component of the

correction while also doubling the magnitude of the nonaxisymmetric component.

The basic shape of this set of twin actuators was obtained from the numerical optimization of an objective function that includes a weighted average of the correctability of the mirror, defined as the ratio between the RMS wavefront error before and after correction, and the stroke, defined as the maximum error amplitude that can be corrected without saturating any actuators. For any design of the actuators, a finite element analysis was carried out to evaluate the objective function. The basic actuator system defined in this way was made more versatile, i.e., able to correct wavefront error modes that are different from the modes for which the basic shape had been obtained, by independently controlling the voltage in each actuation zone, defined by the intersection of the basic actuator shapes. Further improvements, particularly in the correctability of higher-order Zernike components of the error, were achieved by subdividing the central actuation zone into further sets of similarly defined twin-actuator systems.

It has also been shown that reducing the pupil diameter, which can be achieved with a mask or by not coating the edge of the mirror, would improve the correctability, although the scope for doing this in a segmented primary mirror is limited by the appearance of a diffraction pattern and the loss of mirror surface area.

With the proposed approach, several theoretical actuator patterns that can efficiently correct for third-order astigmatism have been designed. Practically feasible modifications of these patterns have then been obtained by imposing a 1 mm constraint on the edge-to-edge distance of neighboring electrodes and a 2 mm wide, clear annulus around the edge. Six actuator patterns with 121, 89, 65, 57, 49, and 41 independent actuators have been obtained. The 41-actuator pattern was built and tested, successfully demonstrating the whole process for mirrors with glass substrate and piezopolymer actuators. Of course, the approach presented is applicable to any type of surface-parallel actuated mirrors and to any combination of active and passive materials, as already demonstrated in a carbon-fiber substrate mirror with piezoceramic actuation layer [16]. The excellent performance of the proposed actuator design method for figure errors dominated by astigmatism makes it well-suited for ultrathin mirrors.

A comparison of the correctability of the 41-actuator based on the present approach, against classically designed actuator patterns including 90-actuator lattice and honeycomb designs, as well as a 41-actuator keystone design, has shown that, in addition to providing superior performance for astigmatism correction, the present approach provides higher or equally higher correctability for 14 out of 25 Zernike modes.

Defense Advanced Research Projects Agency (DARPA) (W31P4Q-14-1-0008); National Aeronautics and Space Administration (NASA).

We thank Xin Ning (Caltech) for help with the optimization algorithm and John Steeves (Caltech) for advice on mirror fabrication. We thank Dr. Harish Manohara (JPL) for providing access to the Microdevices Lab (MDL) cleanroom facilities for sample fabrication. We thank Dr. Risaku Toda (JPL) and Mr. Victor White (JPL) for processing equipment training and usage advice at the MDL. ML acknowledges the support of a postdoctoral grant from the French Defence procurement agency (DGA) held through Aix-Marseille University, France. Financial support from the Keck Institute of Space Studies and the Dow Resnick Bridge program at Caltech is gratefully acknowledged. A part of this research was carried out at the Jet Propulsion Laboratory, California Institute of Technology, under a contract with National Aeronautics and Space Administration (NASA).

## REFERENCES

1. F. Roddier, *Adaptive Optics in Astronomy* (Cambridge University, 1999).
2. C. Grosset-Grange, J.-N. Barnier, C. Chappuis, and H. Cortey, "Design principle and first results obtained on the LMJ deformable mirror prototype," Proc. SPIE **6584**, 658403 (2007).
3. D. Débarre, E. J. Botcherby, T. Watanabe, S. Srinivas, M. J. Booth, and T. Wilson, "Image-based adaptive optics for two-photon microscopy," Opt. Lett. **34**, 2495–2497 (2009).
4. R. J. Zawadzki, S. M. Jones, S. Pilli, D. Y. Kim, S. S. Olivier, and J. S. Werner, "Retinal imaging with a combined adaptive optics/optical coherence tomography and adaptive optics/scanning laser ophthalmoscopy system," Proc. SPIE **7550**, 75500Z (2010).
5. R. H. Freeman and J. E. Pearson, "Deformable mirrors for all seasons and reasons," Appl. Opt. **21**, 580–588 (1982).
6. P.-Y. Madec, "Overview of deformable mirror technologies for adaptive optics and astronomy," Proc. SPIE **8447**, 844705 (2012).
7. M. A. Ealey and J. F. Washeba, "Continuous facesheet low voltage deformable mirrors," Opt. Eng. **29**, 1191–1198 (1990).
8. G. Rodrigues, S. Roose, Y. Stockman, S. Gebhardt, A. Schoenecker, P. Villon, and A. Preumont, "Modular bimorph mirrors for adaptive optics," Opt. Eng. **48**, 034001 (2009).
9. K. Patterson and S. Pellegrino, "Shape correction of thin mirrors," in *52nd AIAA Structures, Structural Dynamics and Materials Conference* (AIAA, 2011).
10. K. Patterson, N. Yamamoto, and S. Pellegrino, "Thin deformable mirrors for a reconfigurable space telescope," in *53rd AIAA Structures, Structural Dynamics, and Materials Conference* (AIAA, 2012).
11. K. Patterson and S. Pellegrino, "Ultralightweight deformable mirrors," Appl. Opt. **52**, 5327–5341 (2013).
12. G. Hickey, T. Barbee, M. Ealey, and D. Redding, "Actuated hybrid mirrors for space telescopes," Proc. SPIE **7731**, 773120 (2010).
13. M. Laslandes, E. Hugot, M. Ferrari, C. Hourtoule, C. Singer, C. Devilliers, C. Lopez, and F. Chazallet, "Mirror actively deformed and regulated for applications in space: design and performance," Opt. Eng. **52**, 091803 (2013).
14. R. N. Wilson, F. Franza, and L. Noethe, "Active optics. I. A system for optimizing the optical quality and reducing the costs of large telescopes," J. Mod. Opt. **34**, 485–509 (1987).
15. M. Postman, T. Brown, K. Sembach, M. Giavalisco, W. Traub, K. Stapelfeldt, D. Calzetti, W. Oegerle, M. Rich, P. Stahl, J. Tumlinson, M. Mountain, R. Soummer, and T. Hyde, "Advanced Technology Large-Aperture Space Telescope: science drivers and technology developments," Opt. Eng. **51**, 011007 (2012).
16. J. Steeves, M. Laslandes, S. Pellegrino, D. Redding, S. K. Bradford, J. K. Wallace, and T. Barbee, "Design, fabrication and testing of active carbon shell mirrors for space telescope applications," Proc. SPIE **9151**, 915105 (2014).
17. J.-C. Sinquin, J.-M. Lurcon, and C. Guillemard, "Deformable mirror technologies for astronomy at CILAS," Proc. SPIE **7015**, 70150O (2008).
18. G. Mendes da Costa Rodrigues, "Adaptive optics with segmented deformable bimorph mirrors," Ph.D. thesis (Universite Libre de Bruxelles, 2010).
19. L. E. Cohan and D. W. Miller, "Integrated modeling for design of lightweight, active mirrors," Opt. Eng. **50**, 063003 (2011).
20. R. J. Noll, "Zernike polynomials and atmospheric turbulence," J. Opt. Soc. Am. **66**, 207–211 (1976).

21. X. Feng, Y. Huang, H. Jiang, D. Ngo, and A. Rosakis, "The effect of thin film/substrate radii on the Stoney formula for thin film/substrate subjected to nonuniform axisymmetric misfit strain and temperature," J. Mech. Mater. Struct. **1**, 1041–1053 (2006).
22. Simulia, Abaqus/Standard, version 6.12.
23. S. Freund and L. Suresh, *Thin Film Materials. Stress, Defect Formation and Surface Evolution* (Cambridge University, 2003).
24. N. Hansen, "The CMA evolution strategy: a comparing review," in *Towards a New Evolutionary Computation. Advances on Estimation of Distribution Algorithms*, J. Lozano, P. Larranaga, I. Inza, and E. Bengoetxea, eds. (Springer, 2006), pp. 75–102.
25. R. Tyson and B. Frazier, *Field Guide to Adaptive Optics*, SPIE Field Guides (SPIE, 2004).
26. V. Mahajan, *Optical Imaging and Aberrations I: Ray Geometrical Optics* (SPIE, 1998).
27. D. Redding, S. Basinger, A. Lowman, A. Kissil, P. Bely, R. Burg, R. Lyon, G. Mosier, M. Femiano, M. Wilson, G. Schunk, L. Craig, D. Jacobson, J. Rakoczy, and J. Hadaway, "Wavefront sensing and control for a Next-Generation Space Telescope," Proc. SPIE **3356**, 758–772 (1998).
28. E. Hecht, *Optics*, 2nd ed. (Addison-Wesley, 1987).
29. T. Coleman and Y. Li, "A reflective Newton method for minimizing a quadratic function subject to bounds on some of the variables," SIAM J. Optim. **6**, 1040–1058 (1996).
30. Thorlabs, Software for WFS Series Wavefront Sensors, V4.2.